Frequency Reconfigurable and Multifunctional Metastructure Regulated by Nematic Liquid Crystal: Broadband Circular to Linear Polarization Converter

Zhen Qiao, Wei Zhang, Yu-Peng Li, Bing-Xing Li,* and Hai-Feng Zhang*

With the tunability of the nematic liquid crystal (NLC), a broadband frequency reconfigurable and versatile metastructure (MS) is proposed and theoretically investigated in this paper, combining circular-to-linear (CTL) polarization conversion (PC) and circular-to-circular (CTC) PC simultaneously. The MS is composed of two via-coupled modules, which can respond differently to the incident waves. Each module is connected utilizing a metal via a column, thus exceedingly enhancing the energy transmission and reducing the loss when transmitting. When the applied bias voltage (V_{bias}) is 0 V, the NCL molecules follow the initial orientation. The MS converts the incident right circular polarized (RCP) waves into linear polarized (LP) waves within 8.11–9.95 gigahertz (GHz) with a relative bandwidth of 20.38% and achieves the PC of left circular polarized (LCP) into RCP waves. As the V_{bias} reaches 20 V, the original operating interval reconfigures and shifts overall toward a lower frequency. The bandwidth of CTL is 7.66–9.02 GHz, and the CTC PC is broadened to 20.20%. Meanwhile, the structure justification is verified, and the inducing mechanism of PC is expounded. Possessing the merits of versatile collaborative processing and wide operating bands, such an MS is promising to be a polarization-controlled application candidate and enrich multifunctional designs.

1. Introduction

With the proliferation of vigorous technological evolution, the extensive application and manipulation of electromagnetic waves (EMWs) are exceedingly crucial currently.[1] The conventional manipulation methods are to utilize the birefringence effect[2] and optical activity of the anisotropic nature materials.[3] Nonetheless, confronted by the dilemma of bulky volume[4] and demanding material restriction,[5] they are fatigued to satisfy the complexity of operating conditions and the trend of miniaturized integration. Fortunately, benefiting from the sub-wavelength periodic structure[6] and the exotic characteristics such as arbitrarily designed permittivity and magnetic permeability,[7] plenty of studies concentrated on metamaterials have sprung up recently and become a hotspot.[8–10] Meanwhile, metastructure (MS) is a three-dimensional case of metamaterial, which processes splendid applications in photon deceleration,[11] remote sensing,[12] energy harvesting,[13] and electromagnetic cloaking,[14] thus unlocking the key bottleneck of manipulation of EM characteristics.

Polarization is an essential category in electromagnetics, electrodynamics, and modern optics, which indicates that the property of the electric field intensity vector changes with time at a given spatial point.[15,16] A polarization converter is foreseen to change the polarization state of incident EMWs after being reflected or transmitted by the MS.[17,18] Exploited to manipulate multiple states of the EMWs, the polarization converter has manifold potential value in transceiver antennas,[19] radar detection,[20] target imaging,[21] and communication systems.[22] In 2007, Hao et al. pioneeringly introduced a reflective polarization converter with an I-beam structure, which utilizes the corresponding discrepancies of electric field and surface currents in the *x*- and *y*-axes to obtain polarization conversion.[23]

The breakthrough and fruitful progress toward the manipulation of EMWs have facilitated intense aspirations in PC. Consequently, the unit structures of PC are sprouting up like wildfire, and novel schemes are gradually being excavated, such as surface plasmonic excitation,[24,25] self-compensating hypersurfaces,[26] and gradient hypersurfaces.[27] It has been confirmed that EMWs process two polarization states. Linear polarized (LP) waves are extensively universal and available, whereas circular polarized (CP) waves are insensitive to atmospheric reflection and absorption and have multiple paths due to their irreplaceable merit of robustness.[28] Considering the significant distinctions in the polarization of EMWs, there is no dispute that it is imperative to design the corresponding polarization converters (i.e., linear-to-linear (LTL or crossed) PC, linear-to-circular (LTC) PC, and circular-to-linear (CTL) PC). To elucidate, Zheng et al. proposed a wideband reflective polarization converter composed of two

Z. Qiao, W. Zhang, Y.-P. Li, B.-X. Li, H.-F. Zhang
College of Electronic and Optical Engineering and College of Flexible Electronics (Future Technology)
Nanjing University of Posts and Telecommunications
Nanjing 210023, P. R. China
E-mail: bxli@njupt.edu.cn; hanlor@njupt.edu.cn

meander lines and one cut wire, which can realize cross-PC within 6.53–12.07 GHz with a relative bandwidth of 59.60% and LTC PC from 13.70 to 15.60 GHz simultaneously.[29] In 2019, by virtue of the equivalent circuit model, Wang et al. successfully demonstrated a dual-band LTC polarization converter whose operating frequency covers the K and Ka bands.[30]

Hitherto, abundant research has been put forward on the fulfillment of diverse polarization converters.[31] Nevertheless, with the advancement of technology, these polarization converters are failing to cope with the increasingly complicated electromagnetic environment due to the restriction of their single function or fixed band.[32] Hence, in-depth studies on the versatile or frequency reconfigurable MS enter a new boom by combining metallic resonators and tunable materials. Considerable methods of regulation include but are not limited to temperature,[33,34] gravity field,[35] illumination,[36,37] and electric field.[38] For instance, Singh et al. experimentally demonstrated and compared the thermal tuning of the fundamental inductive-capacitive resonance, where metals and superconductors are discussed, to active MS resonance tuning.[39] Based on the phase-change material vanadium dioxide and the photosensitive materials silicon and germanium, Guo et al. demonstrated a photoexcited multitasking Janus metasurface in 2022.[40] Moreover, Peng et al. published a multitasking MS based on graphene in 2018, which can convert a broadband absorber into an LTL polarization converter by virtue of altering the chemical potential of graphene.[41] Nematic liquid crystal (NLC) is a widespread-use anisotropic material, whose dielectric constant tensor can be continuously regulated by applied bias voltage (V_{bias}), making it a feasible candidate for tunable materials.[42,43] The cost of NLC is low, and its operating band is vast, ranging from the millimeter-wave band to the terahertz (THz) band.[44] More importantly, NLC is susceptible to the applied electric and magnetic fields, which means that the demand for applied V_{bias} is relatively weak and easy to implement.[45] Accordingly, a host of tunable MSs based on LC are steeply emerging, and the investigations into phase shifters,[46] filters,[47] absorbers,[48] and polarization converters[49] are the pertinent cases in point. An efficient THz reflective phase shifter was exhibited by Yang et al. with a 249° maximum phase shift at the resonant point.[50] Besides, Savo et al. recommended an absorber that can implement spatial light modulation for THz applications, vividly demonstrating the viability of LC-based reconfigurable metastructures.[51] As a result, benefiting from the tunability of NLC, the exploration of reconfigurable metastructures has become increasingly popular currently, thus giving us insight as well.

To the best of our knowledge, there will be 3 dB of energy losses once the LP antenna is utilized in the process of receiving and transmitting CP waves.[52] However, CTL polarization converter schemes are scarcely featured in related reports, and previous works are plagued by the flaws of low transmittance and narrow band. It is a formidable nut to crack, whereas the corresponding solution is imperative considering the universality of the LP receiving antenna. Herein, a broadband reconfigurable and versatile MS is proposed in this paper, which simultaneously combines CTL PC and circular-to-circular (CTC) PC. Based on NLC, the working bandwidth of MS can be a flexible shift by regulating the applied V_{bias}. At $V_{bias} = 0$ V, with a relative bandwidth of 20.38%, a broadband CTL polarization converter can be obtained within 8.11–9.95 GHz. Meanwhile, the proposed MS can convert the LCP into RCP waves in the range of 8.30–9.56 GHz. As V_{bias} gradually increases to 20 V, the operating band of the CTL PC transfers to 7.66–9.02 GHz with a relative bandwidth of 16.31%, meeting the broadband requirements as well. Furthermore, the band of CTC PC is distinctly broadened, ranging from 7.70 to 9.43 GHz with a relative bandwidth of 20.20%. More intuitive operating function information is manifested in **Table 1** below.

The nontrivial properties of the proposed MS can enrich the study of the CTL PC and tunable device, thus foreseeing an alternative way of addressing obstacles like a narrow band, low transmittance, and high loss. And we are committed to the proposal's novel and valuable theoretical research and antecedently explore its essential electromagnetic characteristics and physical mechanism. Therefore, the related experimental processing is not the focus of our attention. Even so, our research group is preparing and gradually working on the various problems brought about by the experimental process. In the near future, follow-up research progress will be reported as soon as possible.

2. Structure Design and Numerical Deduction

Figure 1a illustrates the schematically periodic diagram of the proposed MS, and the two different functions are visually demonstrated by the propagation waves. To be specific, the given versatile MS is capable of converting the incident RCP waves into LP waves in the transmission state, while reflected RCP waves are obtained when LCP waves are incident as well. The stereoscopic view is manifested in Figure 1b after the decomposition of the unit, which is composed of four upper radiation patches, four bottom receiving patches, a metallic middle ground, two glass medium substrates (filled with NLC), and four metal via columns (material gold is utilized for all metallic structures whose conductivity σ_{gold} is 4.561×10^7 S m^{-1}[53]). In Figure 1c, the thickness l and the height h_1 of the glass medium (relative permittivity $\epsilon_{glass} = 4$, loss tangent tan$\epsilon_{glass} = 0$[35]) are 0.1 mm, which is filled with NLC with a thickness of $h_2 = 2.0$ mm. The thicknesses of the patches and metallic middle ground are equal, with $w = 0.1$ mm.

As exhibited in Figure 1d, the upper radiation patches and the bottom receiving patches are identical in shape and are connected by four metal via columns. It is worthwhile to mention that the bottom receiving patches are arranged in two layouts that differ by 90° in direction. The upper radiation patches and the bottom receiving patches are connected up and down through a metal via a column with a radius of $r_3 = 0.4$ mm, and the distance d from the MS's boundary to the center of the patch is selected as $d = 2.0$ mm. Accordingly, the combinations of the upper radiation patch, the bottom receiving patch, as well as the metal via columns are divided into two different modules (Module I and Module II), whose responses are utterly distinct from incident waves. In a nutshell, by rotating 90° of the receiving patches, Module I can receive and convert the incident RCP waves into LCP waves, while Module II is just to receive and propagate RCP waves in comparison. As shown in Figure 1e, the coordinate position relation of metal via columns and middle ground metallic is distinctly explained. The metallic middle ground has the role of preventing the transmission of the co-PC EMWs and acting as a common ground. Four circle holes with a

Table 1. The detailed operating function menu of the proposed metastructure (MS).

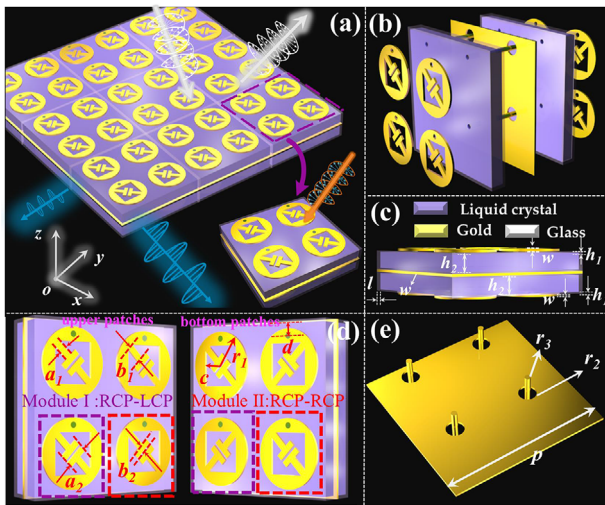| Function	Applied V_{bias}	Operating band [GHz]	Frequency deviation	Relative band [%]	Broadband
CTL PC (transmission)	0 V	8.11–9.95	0.45 GHz (low)	20.38	✓
	20 V	7.66–9.02	0.93 GHz (high)	16.31	✓
CTC PC (reflection)	0 V	8.30–9.56	0.60 GHz (low)	14.11	✗
	20 V	7.70–9.43	0.13 GHz (high)	20.20	✓

Figure 1. Schematic design of the proposed metastructure (MS): a) 3 × 3 array structure diagram, b) the stereoscopic view of the decomposed structure, c) the side view of the given MS, d) the top view and bottom view of the Modules' patches, and e) the related position of the middle ground metallic and metal via columns.
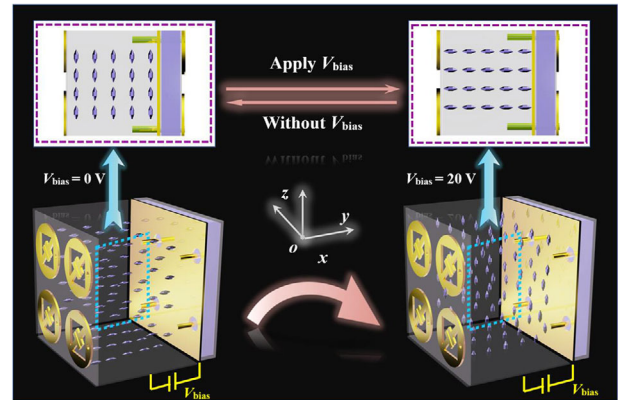

Figure 2. The switch of the orientation of nematic liquid crystal (NLC) molecules and the tunable mechanism of NLC under different V_{bias} (V_{bias} = 0 or V_{bias} = 20 V).

radius of r_2 = 1.2 mm have been dug out on the metallic middle ground to prevent metal contact via columns. Benefiting from the metal via columns, the energy is efficiently transferred to the backside of the given MS and helps to largely diminish the loss.

The anisotropic NLC has been widely investigated due to its low drive voltage requirements, continuously adjustable dielectric properties, small insertion losses, relatively reduced cost, etc. NLC is a tunable material with anisotropy, and its permittivity is related to the orientation of the liquid crystal molecules. In this scheme, the HFUT-HB01 NLC was chosen for another substrate with a permittivity range of ϵ_{min} = 2.49 to ϵ_{max} = 3.63. In a bid to better illustrate the tunable mechanism of NLC, **Figure 2** vividly and intuitively presents the arrangement of NLC molecules under different V_{bias}. The applied V_{bias} controlling the tunable NLC is loaded on both the glass medium substrates and the metallic middle ground. The surface of the inner glass is covered with x-axis rubbed polyimide to ensure that NLC molecules are in the initial state (oriented along the x-axis and parallel to the inner glass surface) when no V_{bias} is applied.[42–44] Therefore, the permittivity tensor of the NLC ($\tan\epsilon$ = 0) can be expressed as:[44–46]

$$\epsilon_1 = \begin{pmatrix} \epsilon_\perp & 0 & 0 \\ 0 & \epsilon_\parallel & 0 \\ 0 & 0 & \epsilon_\perp \end{pmatrix} \tag{1}$$

where the values of $\epsilon_\parallel$ and $\epsilon_\perp$ are 2.49 and 3.63, respectively. After applying the V_{bias} (V_{bias} = 20 V), the dynamic adjustment to the molecular orientation of NLC can be achieved and the permittivity is regulated. Accordingly, the permittivity tensor of the NLC is switched as:[44–46]

$$\epsilon_2 = \begin{pmatrix} \epsilon_\perp & 0 & 0 \\ 0 & \epsilon_\perp & 0 \\ 0 & 0 & \epsilon_\parallel \end{pmatrix} \tag{2}$$

The refractive index tensor of a liquid crystal can be calculated from the permeability tensor and the magnetic permeability tensor of the liquid crystal. Thus, the refractive index tensor of the NLC is related to its permittivity as well.

The modeling and result analysis of the investigated MS is performed with the assistance of commercial simulation software High Frequency Simulation Software (HFSS). The Master-Slave boundary condition is set and the Floquet port is employed for the simulation that the EMWs along the -z-direction is vertically incident on the MS from infinity. More specific parameters on MS can be found in **Table 2** below.

To the best of my knowledge, the CP wave is categorized into the LCP wave and the RCP wave according to their actual direction of rotation. Meanwhile, a CP wave can be combined by virtue of two kinds of LP with the same amplitude and a phase difference of 90°. Actually, an LP wave can be decomposed into two CP waves. In other words, an LP wave can be obtained by virtue of a combination of an LCP wave and an RCP wave with the same amplitude and a certain phase difference. To elucidate,

Table 2. The detailed geometrical dimensions of the investigated metastructure (MS).

Parameters	p	w	l	h_1	h_2	c	d
Values [mm]	22.0	0.2	0.1	0.1	2.0	2.6	2.0
Parameters	r_1	r_2	r_3	a_1	a_2	b_1	b_2
Values [mm]	4.4	1.2	0.4	0.88	2.7	2.8	0.8

considering the incident wave is x-polarized, the derivation process is shown as follows:[52,54,55]

$$E = e_x E = e_x(\frac{1}{2}E + \frac{1}{2}E) = (\frac{1}{2}e_x E + \frac{j}{2}e_y E) + (\frac{1}{2}e_x E - \frac{j}{2}e_y E) \quad (3)$$

The contents in two brackets can be redefined as follows:

$$\frac{1}{2}e_x E + \frac{j}{2}e_y E = e_z E_m e^{j\phi} \quad (4)$$

$$\frac{1}{2}e_x E - \frac{j}{2}e_y E = e_z E_m e^{-j\phi} \quad (5)$$

Hence, Equation (3) can be written as follows:

$$E = e_z E_m e^{j\phi} + e_z E_m e^{-j\phi} \quad (6)$$

As manifested in Equation (6), it is beyond dispute that the LP waves can be decomposed into two different CP waves with opposite rotation and the same amplitude. Correspondingly, an LP wave can be generated by combining the LCP wave and the RCP wave, benefiting from the equal amplitude and the 0° phase difference. Module I and Module II exert extremely different roles in the process of CTL PC, respectively realizing the functions of RCP-RCP and

RCP-LCP in our design. Taking the incident RCP wave as an example, it can be expressed as:[54]

$$E_{in} = \begin{pmatrix} I_x \\ I_y \end{pmatrix} e^{-jkz} = \begin{pmatrix} E_0 \\ j \cdot E_0 \end{pmatrix} e^{-jkz} \quad (7)$$

After shining on the proposed MS, the incident wave is captured by the top patches of Module I and Module II and radiates to the back receiving patch through the metal via columns. In view that the receiving patches differ in the 90° of rotation, Module I can accomplish the RCP-LCP, while Module II is limited to satisfying RCP-RCP. As a result, the decomposed electric fields transmitted by Module I and Module II can be separated and explained as follows:

$$E_{t1} = \begin{pmatrix} t_{1x} \\ t_{1y} \end{pmatrix} e^{-jkz} = \begin{pmatrix} k_x \cdot E_0 \\ j \cdot k_y \cdot E_0 \end{pmatrix} e^{-jkz} \quad (8)$$

$$E_{t2} = \begin{pmatrix} t_{2x} \\ t_{2y} \end{pmatrix} e^{-jkz} = \begin{pmatrix} k_x \cdot E_0 \\ -j \cdot k_y \cdot E_0 \end{pmatrix} e^{-jkz} \quad (9)$$

Once the two CP waves are superimposed, the anticipated LP wave can be generated without fail:

$$E_t = E_{t1} + E_{t2} = \begin{pmatrix} 2 \cdot k_x \cdot E_0 \\ 0 \end{pmatrix} e^{-jkz} \quad (10)$$

Taking the comparison of the amplitude into account, a stunning phenomenon can be noticed that there is times difference between the incident RCP wave and the outgoing LP one. In an effort to further evaluate the performance and efficiency of the given MS, the relative conversion efficiency (RCE) and Ohm insertion loss (OIL) are introduced here by the following equations:[52,54]

$$RCE = \frac{|T_{RCP-LP}|^2}{|R_{RCP-RCP}|^2 + |R_{RCP-LCP}|^2 + |T_{RCP-RCP}|^2 + |T_{RCP-LCP}|^2} \quad (11)$$

$$OIL = 1 - |R_{RCP-RCP}|^2 - |R_{RCP-LCP}|^2 - |T_{RCP-RCP}|^2 - |T_{RCP-LCP}|^2 \quad (12)$$

Herein, T_{i-j} and R_{i-j} are on behalf of the transmission and reflection coefficients. And the i and j are separately referred to as the polarization states of the incident and outgoing waves. It cannot be ignored that the proposed MS is capable of implementing CTC PC as well, and the polarization conversion rate (PCR) is typically utilized in the overall evaluation:[40,41]

$$PCR = \frac{|T_{RCP-LCP}|^2}{|T_{RCP-RCP}|^2 + |T_{RCP-LCP}|^2} \quad (13)$$

3. Simulation Analysis and Physical Mechanism

3.1. Analysis of CTL PC

As illustrated in **Figure 3**, based on the derivation of PC above, the corresponding performance analysis is conducted for the proposed MS when the value of V_{bias} is 0. It can be explicitly observed that the transmission coefficients of $t_{RCP-RCP}$ and $t_{RCP-LCP}$ approximately maintain constant equality in Figure 3a. The $t_{RCP-RCP}$ and $t_{RCP-LCP}$ are over 0.6 in the band of 8.11 to 9.95 GHz with a relative bandwidth of 20.38%, which indicates a highly efficient broadband transmittance. Meanwhile, Figure 3b displays the phase information of the $t_{RCP-RCP}$ and $t_{RCP-LCP}$, and the phase difference between them stays at 0° from start to finish. Accordingly, the LP waves can be composed by virtue of combining the RCP and LCP waves with the same amplitude and a 0° phase difference (see Figure 3c). The amplitude of the synthesized LP waves is nearly approaching the theoretical value, which is the times of the $t_{RCP-LCP}$. The curves of RCE and OIL are plotted in Figure 3d, which can manifest the relative conversion efficiency of the generated LP waves and the energy loss during the process of PC.
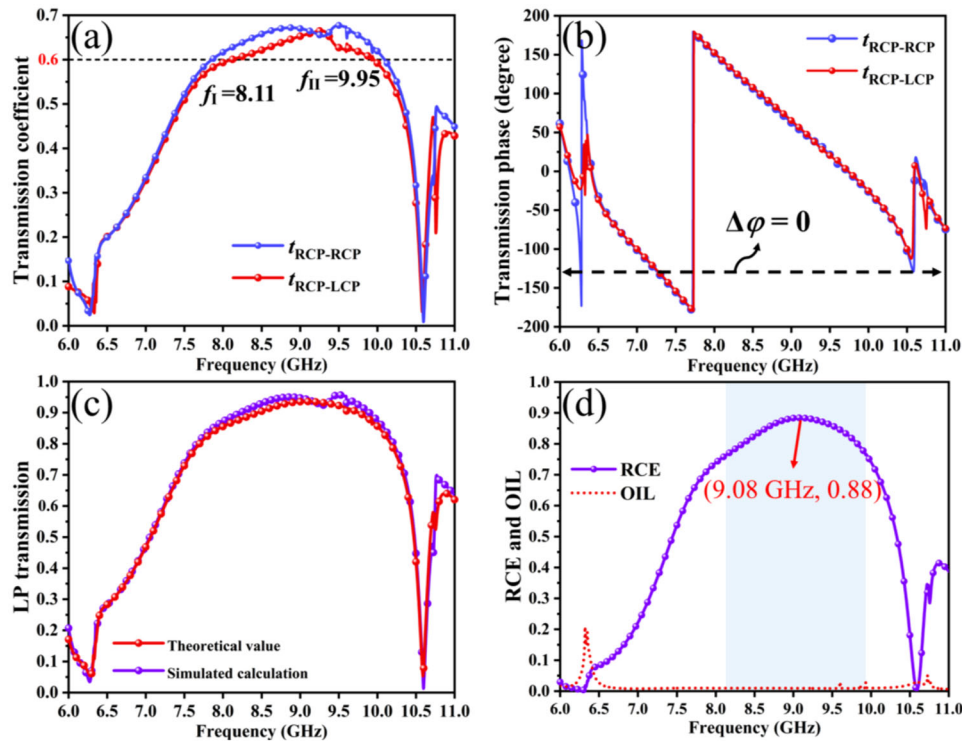
**ADVANCED
SCIENCE NEWS**

www.advancedsciencenews.com

annalen
der **physik**

www.ann-phys.org

Figure 3. The performance curves of the proposed metastructure (MS) without V_{bias}, a) the transmission coefficients of $t_{RCP-RCP}$ and $t_{LCP-RCP}$, b) the transmission phases of $t_{RCP-RCP}$ and $t_{LCP-RCP}$, c) the calculated result of linear polarized (LP) transmission, and d) the curves of relative conversion efficiency (RCE) and Ohm insertion loss (OIL).

The effective region has been marked by the blue blocks. The value of RCE cresting up to 0.88 at 9.08 GHz while the OIL can be ignored with the approximate value of 0, which demonstrates a high efficiency and a low energy loss of this CTL PC.

Similarly, **Figure 4** displays the diverse performance analysis of the given MS as well via adjusting the V_{bias} to 20 V. The transmission coefficients $t_{RCP-RCP}$ and $t_{RCP-LCP}$ are approximately equal in the operating interval of 7.66 to 9.02 GHz, where their value exceeds 0.6, equipped with a constant phase difference ($\Delta\varphi$) of 0°, as presented in Figure 4a,b, respectively. The value of the relative bandwidth is 16.31% under this circumstance, which satisfies the standard of broadband. It is worth noting that the consequences of $t_{RCP-RCP}$ and $t_{RCP-LCP}$ hit a trough that dramatically declines to 0 at 9.50 GHz, which hints at a superior selectivity to the effective EMWs to pass. Subsequently, the LP transmission can be obtained simultaneously with its values over 0.9 in the operating band, which implies a splendid PC of CTL behavior. Apparently illustrated in Figure 4d are RCE and OIL, and the operating interval has been highlighted by the blue blocks as well. The curve of RCE rockets up from 6.0 GHz, reaching the peak of 0.96 at 8.49 GHz. In addition, the values of OIL in the working band are stable and close to 0, implying a superb CTL PC with a barely low loss during transmission.

3.2. Physical Mechanism of CTL PC Behavior

The surface current distributions depicted in **Figure 5** give us an insight into the physical mechanism of CTL PC, which are plotted on different planes at the corresponding resonant points at V_{bias} = 0 and 20 V separately. When the V_{bias} is zero at 9.08 GHz, the surface currents display a consistent trend at the upper radiation patches of both Module I and Module II, which implies that the RCP waves can be efficiently received by the radiation patches. As can be viewed in Figure 5a, there are two major currents marked I_1 and I_2, whose directions are counterclockwise near the middle ground metallic at the outer edge and -γ-axis at the inner verge, respectively, as well as a clockwise weak current I_3. Accordingly, in Figure 5b of the surface current on receiving patches, the main current I_{1a} of Module I is counterclockwise whose direction is isotropic to I_1, which can be inferred that the RCP wave is greatly radiated after transmittance. Nevertheless, the current direction of clockwise I_{1b} of Module II is opposite to I_{1a}, indicating an induced RCP-LCP (convert RCP waves into LCP waves) PC under this condition. More significantly, Module I and Module II are diagonally distributed with a 2 × 2 arrangement, resulting that the accepted RCP waves with equal amplitude by Module I and Module II separately and the amplitude of transformed RCP waves maintaining equivalent as to the radiated LCP waves. Thereby, by combining the output RCP and LCP waves with the same amplitude, a standard LP wave can be ultimately obtained as we desire. Apart from the strongest currents I_1, I_{1a}, and I_{1b}, there are two sets of faint currents whose general directions are anti-parallel, tagged as I_2, I_{2a}, and I_{2b}, as well as I_3, I_{3a}, and I_{3b}. Meanwhile, the I_4 on the middle ground metallic is opposite to the overall downward current on the upper patches (see Figure 5c). Consequently, the anti-parallel currents will induce a magnetic moment m, thus exciting an induced magnetic field H that may trigger PC
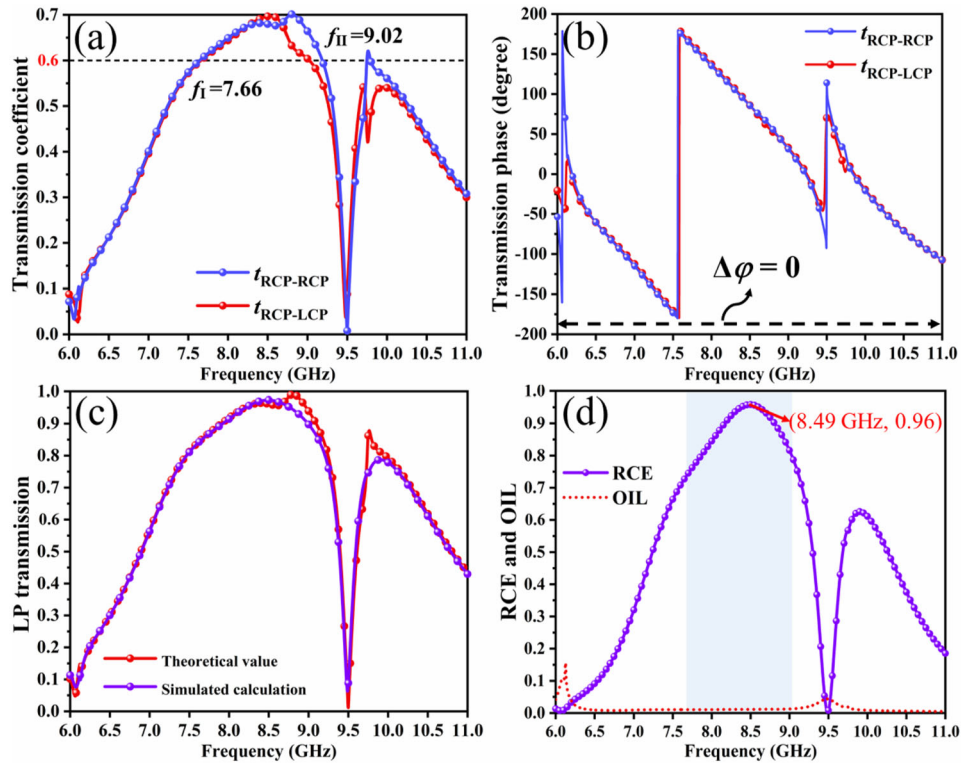
Figure 4. The performance curves of the proposed metastructure (MS) when the V_{bias} is 20 V, a) transmission coefficient of $t_{RCP-RCP}$ and $t_{LCP-RCP}$, b) the transmission phases of $t_{RCP-RCP}$ and $t_{LCP-RCP}$, c) the calculated result of linear polarized (LP) transmission, and d) the curves of relative conversion efficiency (RCE) and Ohm insertion loss (OIL).
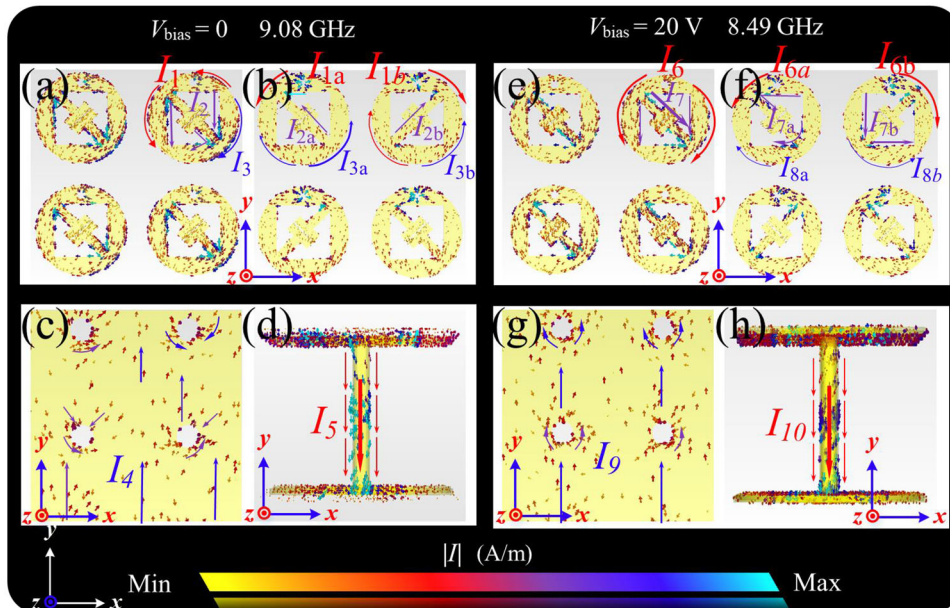

Figure 5. The surface current distributions on different planes including the upper radiation patches, the bottom receiving patches, the middle ground metallic, and the metal via columns at the corresponding resonant points when the V_{bias} is 0 and 20 V separately.

**ADVANCED
SCIENCE NEWS**

www.advancedsciencenews.com
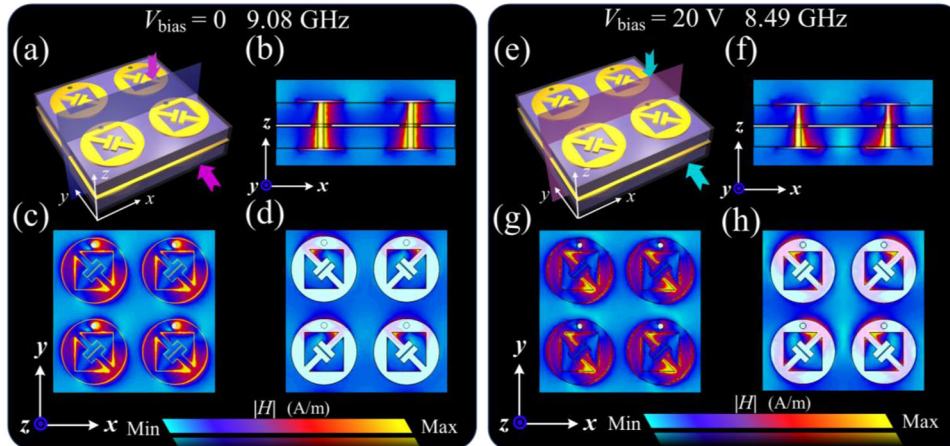
annalen
der **physik**

www.ann-phys.org

Figure 6. The magnetic field distribution on different planes including the metal via-columns, the upper radiation patches and the bottom receiving patches at the corresponding resonant points when the V_{bias} is 0 and 20 V separately.

as well. Next, a *xoz* profile of metal via columns is also plotted. As can be notably observed in Figure 5d, it is through metal via columns that a multitude of intense surface currents labeled I_5 is transmitted from the upper radiation patches to the bottom receiving patches. Therefore, the majority of the EMW energy travels to the backside of the presented MS, accounting for the low loss during the working process of the PC. In view of the fact that the surface currents when $V_{bias} = 20$ V resonant point of 8.49 GHz manifested in Figure 5d,e are analogous in comparison with the above-discussed circumstance, the corresponding physical mechanism and the principle of PC are so similar that it is unessential to repeat them anymore. As stated, the indispensable synthesis of output RCP and LCP waves, which have equal amplitude, and the combination of electric and magnetic coupling are responsible for the realization of CTL PC.

Besides, for the sake of better understanding and verifying the presented MS's superiority of low loss and high transmittance, the magnetic field distribution on different planes is provided in **Figure 6**, which can demonstrate certain information regarding the trace of EMW energy during PC. Figure 6a–d displays the related magnetic field distribution when the V_{bias} is 0 at 9.08 GHz, while the calculated results of $V_{bias} = 20$ V at 8.49 GHz are presented in Figure 6e–h. In particular, the perspective of the inspected *xoz* and *xoy* cross-sections about the magnetic field distributions are stressed by some arrows in Figure 6a,e. As mentioned above in the explanation of currents, there are superabundant currents flowing down through metal via columns, contributing to the especially intense distribution of H in this surrounding region (see Figure 6b,f for details). Accordingly, it can be explicitly concluded that the four metal via-columns hold a crucial role in energy transmission and loss reduction in the course of PC. Subsequently, the rest of the diagrams in Figure 6 are utilized to respectively describe the specific case of H in terms of upper radiation patches and bottom receiving patches. In addition to the metal via columns, the calculated results reveal that vigorous magnetic fields accumulate near the vicinity of MS's diagonal of the upper radiation patches as well. When it comes to the bottom receiving patches, it is worthwhile to note that the distributions of H remain strong at the diagonal. However, Module I and
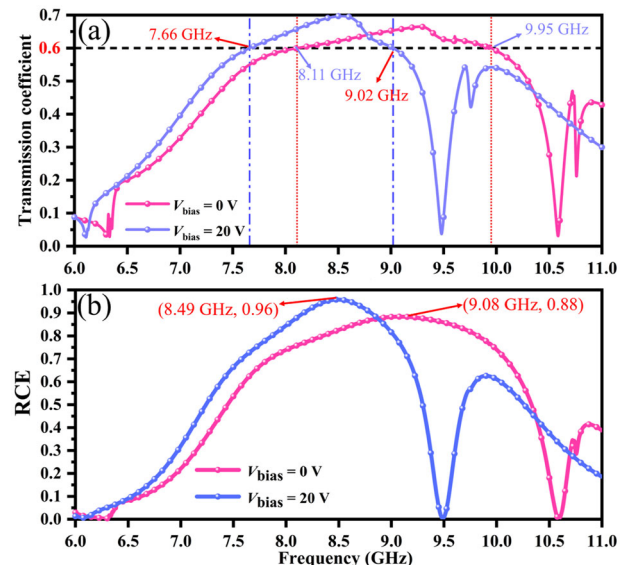

Figure 7. The frequency reconfiguration of the proposed metastructure (MS) when the V_{bias} are 0 and 20 V. a) The results of transmission coefficients of $t_{LCP-RCP}$ and b) the curves of relative conversion efficiency (RCE).

Module II differ by 90° in the structure direction, which signifies that their responses are utterly distinguished from incident RCP waves, thereby leading to an efficient CTL PC.

3.3. Analysis of the Frequency Reconfigurable of CTL PC

To better expound and visualize the frequency reconfiguration of the CTL PC regarding operating interval, the transmission coefficient of $t_{LCP-RCP}$, and RCE are revealed in **Figure 7** below in comparison when the V_{bias} are 0 and 20 V severally. As introduced in Figure 7a, the transmission coefficient is over 0.6 in the band of 8.11–9.95 GHz with a relative bandwidth of 20.38% when there is no V_{bias}. Nonetheless, by virtue of the tunable NLC, the corresponding working bandwidth shifts to a lower frequency overall,
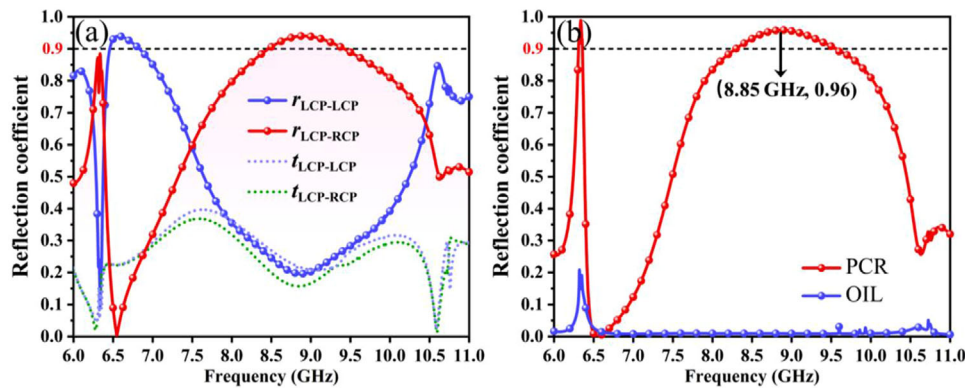
**ADVANCED
SCIENCE NEWS**

www.advancedsciencenews.com

annalen
der **physik**

www.ann-phys.org

Figure 8. The diagrams of the circular-to-circular (CTC) polarization conversion (PC) without V_{bias}, a) the reflection coefficient of $r_{LCP-LCP}$ and $r_{LCP-RCP}$, and b) the calculated curves of polarization conversion rate (PCR) and Ohm insertion loss (OIL).

which ranges from 7.66 to 9.02 GHz with a relative bandwidth of 16.31% when the applied V_{bias} increases to 20 V. The lowest frequency changes from 8.11 to 7.66 GHz, moving by 0.45 GHz, while the highest frequency shifts from 9.95 to 9.02 GHz, with a change of 0.93 GHz. After applying the V_{bias}, the equivalent permittivity of the MS undergoes a change, which is consistent with the alteration of the NLC anisotropic permittivity. The propagation velocity of EMWs is determined by the medium's equivalent permittivity. A decrease in the equivalent permittivity leads to an increase in the propagation velocity. In order to maintain a constant wavelength, the frequency must decrease, which results in a red shift in the operating band. In spite of a reduction in the working band in this situation, the transmission coefficient values creep up to 0.7 at the resonance point of 8.49 GHz, which manifests that almost 98% of EMW energy can be transmitted into the backside of the investigated MS. The peak of RCE moves to a lower frequency from 9.08 to 8.49 GHz in response to the changing trend of transmission efficiency (see Figure 7b). Likewise, the RCE value surges to 0.96 at the resonant point of 8.49 GHz and drops rapidly thereafter when the V_{bias} is 20 V, while the effective band of RCE maintains a wide flat range in the band of 8.11–9.05 GHz in the case of V_{bias} = 0. Hence, it is worthwhile to illuminate that the shift of distinguishing operating interval can be achieved at will by means of controlling the applied V_{bias}. More specifically, the working band is expected to be switched between 7.66 and 9.02 GHz; and 8.11 and 9.95 GHz, which indicates that the applied V_{bias} plays an indispensable switching function in regulating the working states of 7.66–8.11 GHz and 9.02–9.95 GHz.

3.4. Analysis of CTC PC

To ulteriorly demonstrate the performance of the CTC PC of the given MS, which concretely converts the LCP waves into RCP ones, the magnitudes of the cross- and co-polarized reflection coefficients $r_{LCP-RCP}$ and $r_{LCP-LCP}$, as well as the calculated PCR and OIL are exhibited in **Figure 8**a,b. As Figure 8a reveals, the $r_{LCP-RCP}$ is over 0.9 near the resonant point, while the amplitude of the $r_{LCP-LCP}$ remains below 0.2, thus contributing to the formation of the CTC PC. Meanwhile, the transmission response is weak under this circumstance, and the specific manifestation is that the transmission coefficients $t_{LCP-RCP}$ and $t_{LCP-LCP}$ are close to 0.2 as

well. Accordingly, a narrow band of PCR (over 0.9) appears in the range of 8.30–9.56 GHz with a relative bandwidth of 14.11%, as presented in Figure 8b, with PCR values rising up to 0.96 at 8.85 GHz and OIL values fitting snugly into 0.

In like manner, **Figure 9** is plotted to illustrate the tunability of NLC with regard to the CTC PC when the applied V_{bias} is 20 V. Compared to Figure 8 without the V_{bias}, there are distinct enhancements in the overall curves and metrics in Figure 9, with a mild frequency deviation simultaneously. It can be obviously observed that the working band of $r_{LCP-RCP}$ (over 0.9) is widening instead of being a mere single resonant point anymore, where the other coefficients are mostly less than 0.2 in this band, facilitating a broader CTC PC of the proposed MS (see Figure 9a). In Figure 9b, the calculated PCR is stable above 0.9 in the working scope of 7.70–9.43 GHz with a 20.20% relative bandwidth, with the values cresting up to almost 1 at the two corresponding resonant frequencies separately. Moreover, the implications of OIL can be neglected in that the values are exceedingly close to 0.

3.5. Physical Mechanism of CTC PC Behavior

In light of that the principle of CTC PC is similar, hence, the circumstance of V_{bias} = 20 V is opted to elucidate the mechanism. The corresponding surface current distributions are manifested in **Figure 10**, which respectively describes the concrete situation of two different resonant points at 8.41 and 9.27 GHz (PCR = 0.99 and 0.98, respectively) with regard to the CTC PC in the reflection state. At 8.41 GHz, the anti-parallel currents generated between the upper radiation patches and middle ground metallic caused by I_1 and I_2 will induce a magnetic moment m, thus triggering an induced magnetic field H_1 (see Figure 10a,b). To the best of our knowledge, the incident RCP wave can be decomposed into two orthogonal LP waves. Therefore, it is reasonable to decompose it into E_{i1} and E_{i2}, whose directions are separately parallel and perpendicular to H_1. It is noted that the orientation of the equivalent E_1 induced by H_1 is reversed compared to the part of incident E_{i2}, and the magnitude of E_1 generated by magnetic coupling is stronger than E_{i2}. As a result, the original E_{i2} perpendicular to H_1 finally flips 180°, while the E_{i1} parallel to H_1 stays the same, thus contributing to the realization of broadband and low-loss CTC PC. In like manner, as exhibited in Figure 10c,d,
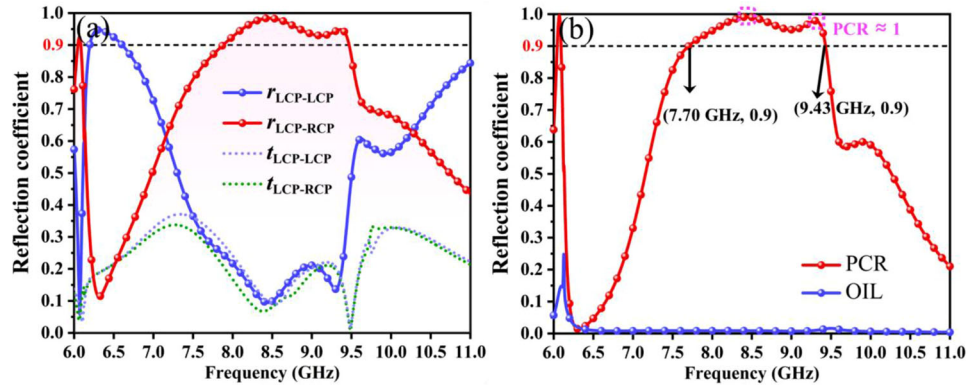
Figure 9. The diagrams of the circular-to-circular (CTC) polarization conversion (PC) when the V_{bias} is 20 V. a) The reflection coefficient of $r_{LCP\text{-}LCP}$ and $r_{LCP\text{-}RCP}$ and b) the calculated curves of polarization conversion rate (PCR) and Ohm insertion loss (OIL).
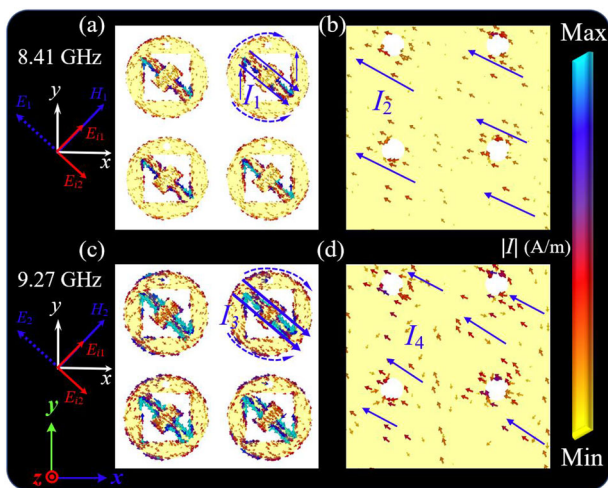

Figure 10. The surface current distributions (a) on the upper radiation patches and (b) middle ground metallic at two peak resonant points at 8.41 GHz when the V_{bias} is 20 V. Surface current distributions (c) on the upper radiation patches and (d) on the middle ground metallic at 9.27 GHz peak resonant point when V_{bias} is 20 V.

there is a circulating current formed by I_3 and I_4 at 9.27 GHz, which can give rise to the magnetic moment m as well, and the derivation process of CTC PC is exactly identical to 8.41 GHz.

3.6. Analysis of the Frequency Reconfigurable of CTC PC

Subsequently, in a bid to elucidate the frequency reconfigurable of the CTC PC, **Figure 11** is depicted to provide more insights into the shift in frequency when the V_{bias} are 0 and 20 V, respectively. With a relative bandwidth of 14.11% and a peak PCR value of 0.96 at 8.85 GHz, the investigated design fulfills a narrow operating interval (PCR > 0.9) of 8.30–9.56 GHz when the original V_{bias} is 0. When the V_{bias} is adjusted to 20 V, it is beyond dispute that there is an apparent optimization in terms of the frequency band accompanied by a slight red shift, benefiting from the permittivity change of the tunable NLC. Spanning from 7.70 to 9.43 GHz, the working scope is better promoted, and the relative bandwidth is broadened to 20.20% from 14.11%, which caters to the metric
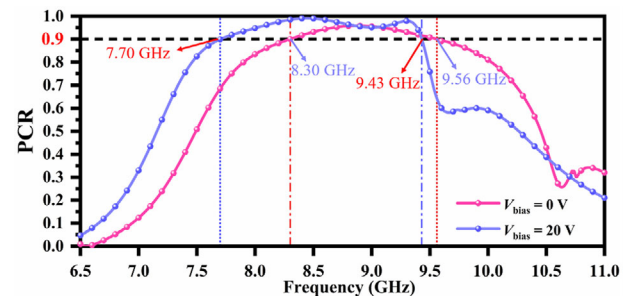

Figure 11. The frequency deviation of polarization conversion rate (PCR) with regard to circular-to-circular (CTC) polarization conversion (PC) when the V_{bias} are 0 and 20 V respectively.

of broadband. Chances are that the redshift of the frequency window can be attributed to the change in the equivalent permittivity of the metastructure. The variation in the equivalent permittivity will affect the propagation velocity of EMWs, resulting in a change in frequency to maintain the same wavelength, which is the redshift observed in the frequency window. The variation at the highest frequency is relatively minor, shifting from 9.56 to 9.43 GHz, while at the lowest frequency, it widens significantly from 8.30 to 7.70 GHz. Meanwhile, the values of PCR within the effective bandwidth fluctuate near 1, except for the concave point value of 0.96 at 8.85 GHz, reflecting the overall elevation in PCR level benefiting from the tunable NLC. The operating band can be switched between 8.30 and 9.56 GHz; and 7.70 and 9.43 GHz via regulating the applied V_{bias}, thus achieving on-off control of working states ranging from 7.70 to 8.30 GHz and 9.43 to 9.56 GHz.

4. Parameter Discussions

4.1. Angular Stability Analysis

As illustrated in the contours of **Figure 12**, the calculated results of $t_{LCP\text{-}RCP}$ and PCR at different angles are all exhibited when the V_{bias} are at the states of 0 and 20 V, respectively, to further investigate the independence of the presented MS in terms of incident angle. Chances are that the device will facilitate its wide application in current hypercomplex communication environments once it possesses splendid angular stability. Under the
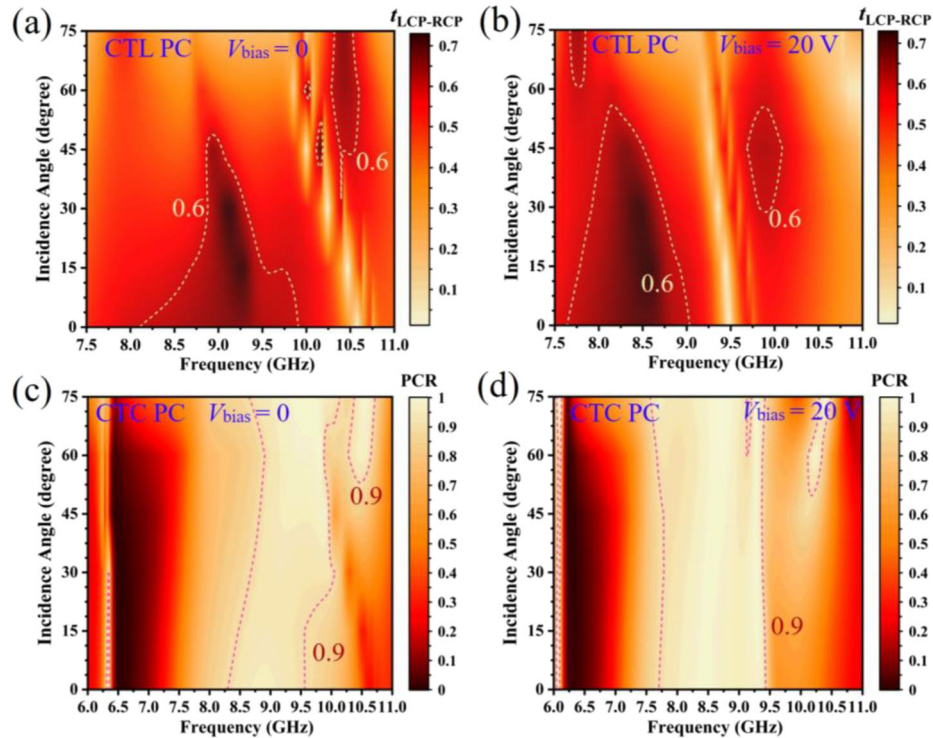
ADVANCED
SCIENCE NEWS
www.advancedsciencenews.com

annalen
der **physik**
www.ann-phys.org

Figure 12. Angular stability (varying from 0° to 75°) of a) the coefficient of $t_{LCP\text{-}RCP}$ when V_{bias} is set 0 and b) the coefficient of $t_{LCP\text{-}RCP}$ as V_{bias} gradually increases to 20 V with regard to CPT polarization conversion (PC). The polarization conversion rate (PCR) at different incident angles (varying from 0° to 75°) for c) the CPC PC when V_{bias} is set 0, and d) the CPC PC with the value of V_{bias} = 20 V, respectively.

meticulous observation of Figure 12a, in spite of a sluggish attenuation with regard to the lower frequency, the magnitude of $t_{LCP\text{-}RCP}$ remains essentially stable and meets the metric of broadband when the incident angle varies from 0° to 15°. Nonetheless, as the incident angle increases, the origin operating band gradually decreases and eventually disappears at a 45° angle. Meanwhile, it is worthwhile to note that the proposed MS presents outstanding characteristics of angular stability (more than 40°) in terms of $t_{LCP\text{-}RCP}$ around the frequency of 10.5 GHz instead. Similarly, in Figure 12b, with the same trend compared to Figure 12a, when the V_{bias} is set to 20 V, the initial working scope of 7.66–9.02 GHz continuously suffers degradation and obliterates as the incident angle increases to 55°. In a nutshell, the proposed MS can exhibit a certain degree of angular stability under mild changes in incident angles (less than 15°).

For the case of CTC PC, the stability of the incident angle concerning the V_{bias} of 0 and 20 V is depicted in Figure 12c,d, respectively. It can be seen in Figure 12c that a trivial fluctuation with respect to frequency bandwidth under this condition, accompanied by a slight blue shift as the incident angle surges up to 75°, indicates excellent angle stability. As to Figure 12d, although there is deterioration at 9.25 GHz at incidence angles greater than 60°, it manifests the optimal angular stability on the grounds that the working band consistently maintains itself virtually unchanged. In light of the aforementioned analysis, the investigated MS is anticipated to be utilized for comprehensive and potential application values on multiple practical occasions, such as wavefront detection, biomedical imaging, and atmospheric environment detection.

4.2. Key Parameters of Impact Analysis

To ultimately obtain the optimal performance, the geometrical parameters of the given MS are optimized by simulation software. The variations of behavior curves concerning two critical parameters with regard to CTL PC and CTC PC are separately displayed in **Figures 13** and **14**, which comprise the related parameters b_2 of the horizontal metal strip and h_2 of the thickness of NLC. As can be found in Figure 13a, there are significant changes in the transmission coefficient when the values of b_2 are 0.75 and 0.80 mm, respectively, specifically in terms of the bandwidth and the peak value. With the band varying from 8.51–9.98 to 8.11–9.95 GHz, a superior advantage appears in the operating band when b_2 changes from 0.75 to 0.80 mm, highlighted by a purple curve, in spite of a sacrifice in the peak value. Nonetheless, there is a general deterioration in the aspect of transmission coefficients greater than 0.6, resulting in a reduced effective bandwidth. Furthermore, when taking bandwidth and peak into account, it is feasible and sensible to opt b_2 as 0.80 mm for incident RCP beams rather than 0.75 or 0.85 mm (see Figure 13b,c). Figure 13d reveals that when b_2 varies among 0.75, 0.80, and 0.85 mm with the same ascending slope, the curve of b_2 = 0.80 mm owns the widest bandwidth, and the values of PCR fluctuate around 0.95 to 1 within the effective band, while there are both slots under the two other circumstances. Therefore, to sum up, b_2 = 0.80 mm is given top priority via comprehensive consideration of excellent performance and operating interval.

The ensuing part concentrates on the discussions about the influence of parameter h_2, which is vividly manifested in Figure 14.
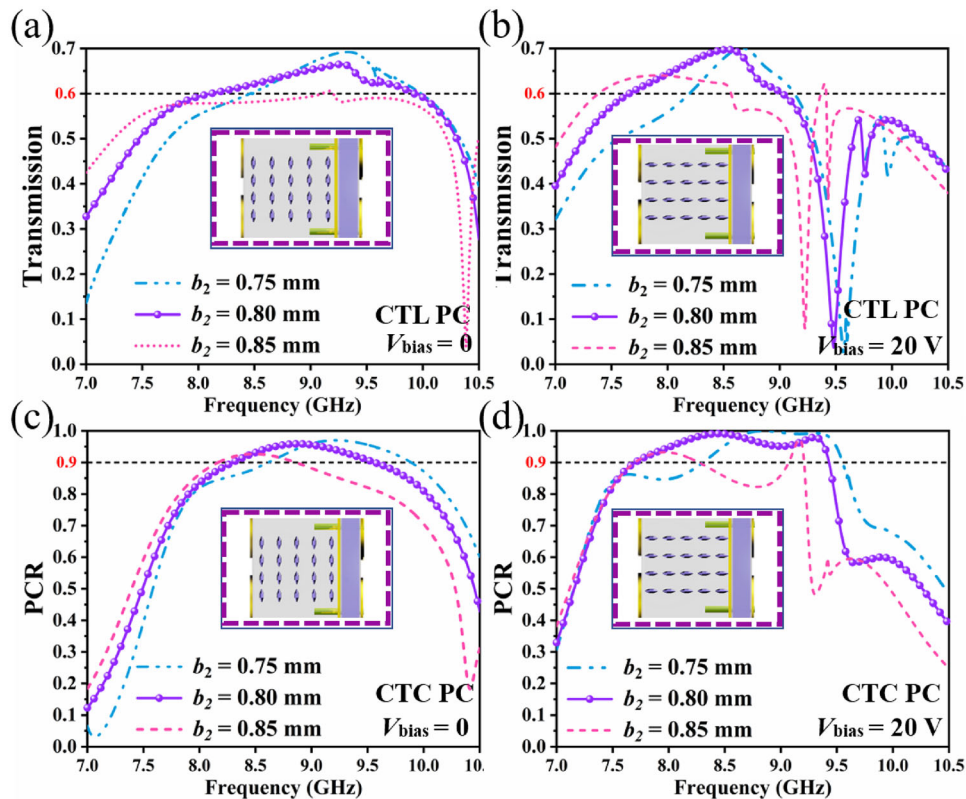
**ADVANCED
SCIENCE NEWS**

www.advancedsciencenews.com

annalen
der **physik**

www.ann-phys.org

Figure 13. The calculated transmission coefficients of circular-to-linear (CTL) polarization conversion (PC) when the V_{bias} are a) 0, b) 20 V in the case of b_2 varying from 0.75 to 0.85 mm. The parameter discussion of b_2 concerning circular-to-circular (CTC) PC when the V_{bias} is c) 0, d) 20 V in the case of b_2 varying from 0.75 to 0.85 mm.

It can be seen in Figure 14a that the effective band (over 0.6) of the transmission coefficient is obviously expanded at the higher band when h_2 is 2.0 mm compared to $h_2 = 1.7$ and 2.3 mm, which is mainly embodied in the range of 9.58–9.95 GHz. Moreover, there is an undeniable advantage under this circumstance of $h_2 = 2.0$ mm when simultaneously taking both bandwidth and transmittance into account. By virtue of the more comprehensive performance and the more distinct frequency deviation, it is beyond dispute that $h_2 = 2.0$ mm will be given top priority consideration. As for the PC of CTC exhibited in Figure 14c,d when h_2 varies from 1.7 to 2.3 mm, it is obvious that a significant deterioration will occur both in bandwidth and performance with $h_2 = 2.3$ mm, which is inferior to the other two values. At the left verge of the PCR effective band (over 0.9), there is an evident red-shift with the value of h_2 gradually increasing, but little difference in the origin of this band. The original beginning frequency point maintains unchanged at the left verge of the PCR effective band (over 0.9), despite an evident red-shift as the value of h_2 gradually increases (see Figure 14c). Meanwhile, the right side dilates to 9.56 and 10.35 GHz, resulting in the operating interval expanding from 14.11% to 21.98%. As demonstrated in Figure 14d, the relative band is roughly equal with a slight blue shift when h_2 is 1.7 and 2.0 mm, respectively. Nonetheless, the corresponding performance is more stable in the working band when h_2 is 2.0 mm, in that the PCR values fluctuate over 0.95 and plunge sharply within 9.43–9.55 GHz, which indicates a superb

switching effect and better selectivity. In a nutshell, $h_2 = 2.0$ mm is deemed to be the optimal value for the presented design.

The equivalent circuit theory[56,57] can provide insight into the physical mechanisms of frequency redshift, the trend of $t_{LCP-RCP}$, and PCR with parameter changes. The corresponding transmission and reflection mode characteristics are determined by electromagnetic response of MS when EMWs are incident upon a MS. Based on equivalent circuit theory in general, the MS can be equivalent to a series RLC resonant circuit. Altering the structural or electrical parameters of the metamaterial, such as its changes in the geometric shape or component properties, can cause changes in the equivalent permittivity and permeability of the metamaterial, which, in turn, affect its response and transmission characteristics to incident EMWs. Taking h_2 of the NLC thickness as an example, as h_2 grows, the equivalent capacitance C in the RLC equivalent circuit augments, while the equivalent inductance L and resistance R typically diminish. This is attributed to the enlarged distance between the capacitor plates, which increases the equivalent capacitance, leading to a concomitant decrease in the MS's equivalent inductance and resistance. As a consequence, the corresponding $t_{LCP-RCP}$ and PCR will alter once the parameters change. This change in the equivalent permittivity affects the propagation velocity of EMWs as well, resulting in a decrease in frequency to maintain the same wavelength, which is the redshift observed in the frequency window. (**Figure 15**)
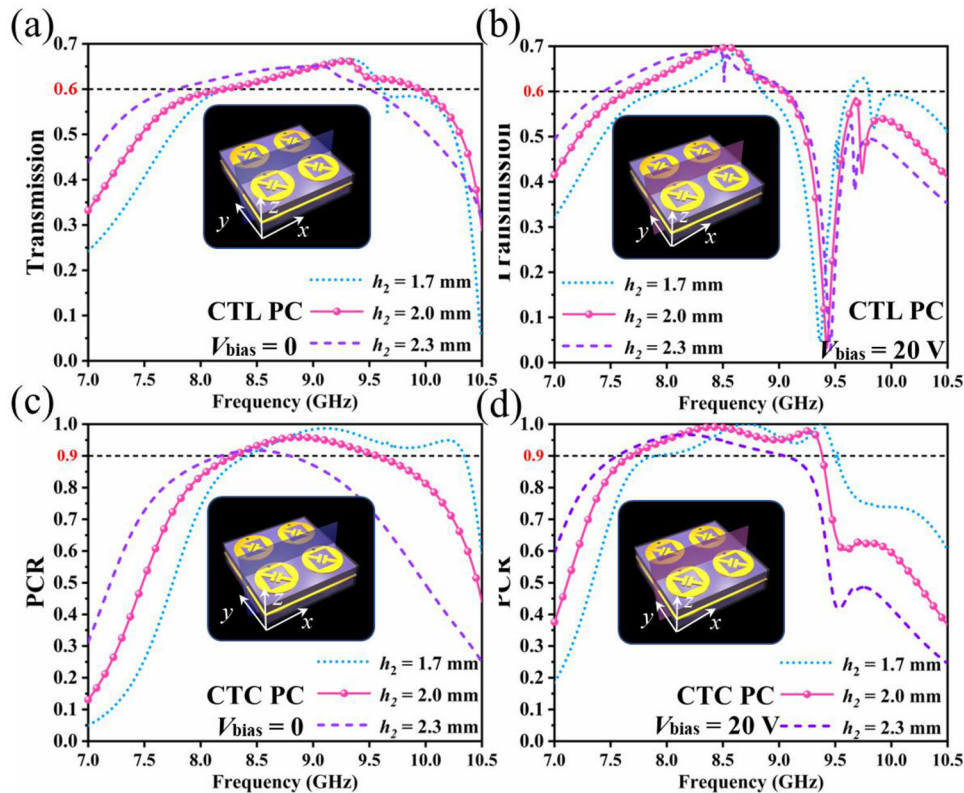
Figure 14. The results of transmission coefficient of CTL PC when the V_{bias} is a) 0, b) 20 V in the case of h_2 varying from 1.7 mm to 2.3 mm. The parameter discussion of h_2 concerning CTC PC when the V_{bias} is c) 0, d) 20 V in the case of h_2 varying from 1.7 mm to 2.3 mm.
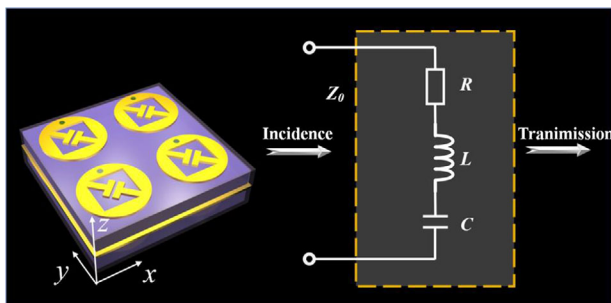

Figure 15. The equivalent circuit model of the proposed metastructure.

4.3. Potential Methods of Experimental

For planar metamaterials, the methods of optical lithography are mainly used.[58] As one of the most important steps to fabricate micro nanostructures, optical lithography generally includes wafer cleaning and drying, coating photoresist, prebaking, exposure, post-baking, development, hard baking, and other processes.[59] Among them, exposure and development is the most critical step in the lithography process, which is directly related to the accuracy of metal nanostructures. The metal resonator pattern of upper radiation patches and bottom receiving patches can be defined by photolithography, and gold can be deposited by E-beam evaporation,[58] which is common in the fabrication of metasurfaces and metastructures.

The preparation method generally includes the following steps: The material of NLC is first prepared by chemical reaction, and then the liquid crystal material is heated to a certain temperature to melt it.[42] After the liquid crystal is completely melted, it is rapidly cooled and an external electric field is applied to arrange the liquid crystal molecules into a nematic structure. The preparation process requires strict control of the heating and cooling rates as well as the application of the electric field to obtain the desired nematic liquid crystal structure.[44] The liquid crystal samples are then tested for physical and optical properties to determine the nature and application potential of the nematic liquid crystal phase.[44]

4.4. Comparisons with Other Reported Devices

Finally, to exhibit definite innovation concerning the presented MS based on NLC, **Table 3** is given to make a comparison between NLC and other phase change materials, such as vanadium dioxide, graphene,[66,67] and silicon, which helps us better comprehend the situation of related work. Phase change materials, external variables, adjustment objects, tunable functions, or shiftable operating bands in different works are listed overall. It is clear that the devices mentioned above perform admirably. However, the NLC-based MS we proposed has irreplaceable advantages as well, such as multifunctionality and distinct frequency deviation.

Table 3. Comparisons between this work and reported switchable and multitasking devices.

Refs.	Materials	External variables	Adjustment object	Change of performance parameters (functionality and working band)[a]
[60]	Vanadium dioxide (THz)	Thermal	Functionality	①LTL PC: PCR > 0.9 (0.91–2.15) ②LTC PC: AR < 3 dB (1.07–1.67)
[61]			Functionality	①LTL PC: PCR > 0.9 (0.69–1.38) ②Absorber: AB > 0.9 (0.67–0.95)
[62]	Graphene (THz)	Voltage	Functionality	①LTL PC: PCR > 0.9 (0.40–0.95) ②LTC PC: AR < 3 dB (0.47–0.67)
[63]			Working band	Multi-band absorber: Reconfigure the band of 1, 2.45 and 2.82 THz
[64]	Silicon (THz)	Photo-excited	Functionality	①LTL PC: PCR > 0.9 (2.01–2.56) ②Absorption peaks: 1.98 and 3.24 THz
[65]			Functionality	①LTL PC: PCR > 0.9 (0.96–1.47) ②Absorber: AB > 0.9 (0.75–1.73)
[49]	NLC (GHz)	Voltage	Working point	Spatial light modulator: The absorption point shifts from 3.67 to 3.42 THz
[50]			Working point	Absorber: The central frequency is tuned from 11.04 to 10.21 GHz
This work	NLC (GHz)	Voltage	Working band	①CTL PC: $t_{RCP\text{-}LCP}$ > 0.6 (8.11–9.95) → (7.66–9.02) GHz ②CTC PC: PCR > 0.9 (8.30–9.56) → (7.70–9.43) GHz

[a] AR = Axial ratio, AB = absorption band.

5. Conclusion

In summary, a frequency reconfigurable and multifunctional MS based on NLC is theoretically proposed, which can implement broadband CTL PC and CTC PC simultaneously as well as a distinct frequency deviation by the tunable permittivity of NLC when the applied V_{bias} is adjusted. The MS is composed of two different types of modules, which distribute diagonally and respond completely differently to the incident RCP waves. Module I is expected to receive and convert the incident RCP waves into LCP ones, while Module II is merely expected to receive RCP waves compared to Module I, thus leading to the generation of LP waves. When it comes to CTL PC, the broadband operating interval shifts from 8.11–9.95 to 7.66–9.02 GHz with relative bandwidths of 20.38% and 16.31%, respectively, when the V_{bias} is adjusted from 0 to 20 V. Meanwhile, there is an apparent optimization in terms of the bandwidth performance of CTC PC, accompanied by a red shift in the working band. The corresponding working scope can be switched between 8.30–9.56 and 7.70–9.43 GHz via regulating the applied V_{bias}. The surface current and magnetic field distributions are introduced to interpret the mechanisms of PC, and conventional angular stability analysis and key parametric discussions are investigated in detail as well. Such a novel design of the frequency reconfigurable and multifunctional MS can manifest a promising prospect and find potential applications in satellite communication systems, antenna fields, and remote sensors.

Conflict of Interest

The authors declare no conflict of interest.

Data Availability Statement

The data that support the findings of this study are available on request from the corresponding author. The data are not publicly available due to privacy or ethical restrictions.

[1] M. Kuwata-Gonokami, N. Saito, Y. Ino, M. Kauranen, K. Jefimovs, T. Vallius, *Phys. Rev. Lett.* **2005**, *95*, 227401.

[2] S. T. Oh, W. T. Han, U. C. Paek, Y. Chung, *Opt. Express* **2004**, *12*, 724.

[3] Y. Joly, S. P. Collins, S. Grenier, H. C. N. Tolentino, M. D. Santis, *Phys. Rev. B.* **2012**, *86*, 220101.

[4] N. Yu, F. Capasso, *Nat. Mater.* **2014**, *13*, 139.

[5] R. D. King-Smith, D. Vanderbilt, *Phys. Rev. B.* **1993**, *47*, 1651.

[6] T. J. Cui, M. Q. Qi, X. Wan, J. Zhao, Q. Cheng, *Light: Sci. Appl.* **2014**, *3*, e218.

[7] V. A. Fedotov, P. L. Mladyonov, S. L. Prosvirnin, A. V. Rogacheva, Y. Chen, N. I. Zheludev, *Phys. Rev. Lett.* **2006**, *97*, 167401.

[8] N. I. Zheludev, Y. S. Kivshar, *Nat. Mater.* **2012**, *11*, 917.

[9] M. Pan, Z. C. Su, Z. F. Yu, P. H. Wu, H. G. Jile, Z. Yi, Z. Q. Chen, *Results Phys.* **2020**, *19*, 103415.

[10] J. Wu, Y. J. Cheng, Y. Fan, *IEEE. Trans. Antennas Propag.* **2015**, *64*, 535.

[11] E. Distante, P. Farrera, A. Padron-Brito, D. Paredes-Barato, G. Heinze, H. D. Riedmatten, *Nat. Commun.* **2017**, *8*, 14072.

[12] W. S. Chu, S. M. Kim, X. P. Wu, L. Wen, M. C. Oh, *J. Lightwave Technol.* **2016**, *34*, 2170.

[13] M. Karaaslan, M. Bagmaci, E. Unal, O. Akgol, C. Sabah, *Opt. Commun.* **2017**, *392*, 31.

[14] G. T. Ounbe Tekam, V. Ginis, J. Danckaert, P. Tassin, *Appl. Phys. Lett.* **2017**, *110*, 083901.

[15] J. Y. Duclos, J. Esteban, D. Ray, *Econometrica* **2004**, *72*, 1737.

[16] H. Dorrah, N. A. Rubin, A. Zaidi, M. Tamagnone, F. Capasso, *Nat. Photonics* **2021**, *15*, 287.

[17] X. Gao, X. Han, W. P. Cao, H. O. Li, H. F. Ma, T. J. Cui, *IEEE. Trans. Antennas Propag.* **2015**, *63*, 3522.

[18] P. C. Wu, W. M. Zhu, Z. X. Shen, P. H. J. Chong, W. Ser, D. P. Tsal, A. Q. Liu, *Adv. Opt. Mater.* **2017**, *5*, 1600938.

[19] J. Yang, S. T. Chen, M. Chen, J. C. Ke, M. Z. Chen, C. Zhang, R. Yang, X. Li, Q. Cheng, T. J. Cui, *IEEE. Trans. Antennas Propag.* **2020**, *69*, 806.

[20] Y. C. Yuan, C. C. Lu, A. Y. K. Chen, C. H. Tseng, C. T. M. Wu, *IEEE. Trans. Microwave Theory Tech.* **2019**, *67*, 5429.

[21] S. Mukherjee, Z. Su, L. Udpa, S. Udpa, A. Tamburrino, *IEEE Sens J.* **2019**, *19*, 4962.

[22] G. B. Xavier, G. V. D. Faria, G. P. Temporao, J. P. V. D. Weid, *Opt. Express* **2008**, *16*, 1867.

[23] J. Hao, Y. Yuan, L. X. Ran, T. Jiang, J. A. Kong, C. T. Chan, L. Zhou, *Phys. Rev. Lett.* **2007**, *99*, 063908.

[24] P. Wang, M. E. Nasir, A. V. Krasavin, W. Dickson, Y. L. Jiang, A. V. Zayats, *Acc. Chem. Res.* **2019**, *52*, 3018.

[25] J. T. Heiden, F. Ding, J. Linnet, Y. Q. Yang, J. Beermann, S. I. Bozhecolinyi, *Adv. Opt. Mater.* **2019**, *7*, 1801414.

[26] S. J. Ma, Y. G. Bi, Q. H. Guo, B. Yang, O. You, J. Feng, H. B. Sun, S. Zhang, *Science* **2021**, *373*, 572.

[27] F. Pacard, M. Ritore, *J. Differ. Geom.* **2003**, *64*, 359.

[28] Q. Liang, T. Wang, Z. Lu, Q. Sun, Y. Fu, W. Yu, *Adv. Opt. Mater.* **2013**, *1*, 43.

[29] Q. Zheng, C. Guo, J. Ding, *IEEE Antennas Wireless Propag.* **2018**, *17*, 1459.

[30] H. B. Wang, Y. J. Cheng, *IEEE Trans. Antennas Propag.* **2019**, *67*, 4296.

[31] Nemati, Q. W., M. H. Hong, J. H. Teng, *Opto-Electron. Adv.* **2018**, *1*, 18000901.

[32] H. Zhang, X. C. He, D. Zhang, H. F. Zhang, *Opt. Express* **2022**, *30*, 23341.

[33] Y. B. Zhang, P. H. Wu, Z. G. Zhou, X. F. Chen, Z. Yi, J. Y. Zhu, T. S. Zhang, H. G. Jile, *IEEE Access* **2020**, *8*, 85154.

[34] D. W. Zeng, S. Zong, G. Q. Liu, W. Yuan, X. S. Liu, Z. Q. Liu, *Opt. Express* **2022**, *30*, 39736.

[35] L. Zeng, H. F. Zhang, G. B. Liu, T. Huang, *Plasmonics* **2019**, *14*, 1347.

[36] J. C. Zhao, Y. Z. Cheng, Z. Z. Cheng, *IEEE Photonics J.* **2018**, *10*, 4600210 .

[37] G. Q. Liu, M. L. Liu, G. L. Fu, X. S. Liu, Z. Q. Liu, *Opt. Express* **2022**, *30*, 26597.

[38] C. Huang, C. L. Zhang, J. N. Yang, B. Sun, B. Zhao, X. G. Luo, *Adv. Opt. Mater.* **2017**, *5*, 1700485.

[39] R. Singh, D. R. Chowdhury, J. Xiong, H. Yang, A. K. Azad, A. J. Taylor, Q. X. Jia, H. T. Chen, *Appl. Phys. Lett.* **2013**, *103*, 061117.

[40] Z. H. Guo, Y. Z. Sun, L. Zeng, H. F. Zhang, *Ann. Phys.* **2022**, *534*, 2100499.

[41] L. Peng, X. Jiang, S. Li, *Nanoscale Res. Lett.* **2018**, *13*, 385.

[42] G. Isic, B. Vasic, D. C. Zografopoulos, R. Beccherelli, R. Gajic, *Phys. Rev. Appl.* **2015**, *3*, 064007.

[43] D. Shrekenhamer, W. C. Chen, W. J. Padilla, *Phys. Rev. Lett.* **2013**, *110*, 177403.

[44] J. F. Lv, C. Ding, F. Y. Meng, J. Q. Han, T. Jin, Q. Wu, *Liq. Cryst.* **2021**, *48*, 1438.

[45] F. L. Zhang, W. H. Zhang, Q. Zhao, J. B. Sun, K. P. Qiu, J. Zhou, D. Lippens, *Opt. Express* **2011**, *19*, 1563.

[46] Y. Y. Ji, F. Fan, S. T. Xu, J. P. Yu, S. J. Chang, *Nanoscale* **2019**, *11*, 4933.

[47] S. T. Xu, F. Fan, Y. H. Wang, T. Z. Yang, H. Z. Cao, S. J. Chang, *Appl. Opt.* **2021**, *60*, 9530.

[48] R. X. Wang, L. Li, J. L. Liu, F. Yan, F. J. Tian, J. Z. Zhang, W. M. Sun, *Opt. Express* **2017**, *25*, 32280.

[49] M. Wang, X. K. Wang, P. Han, W. F. Sun, S. F. Feng, J. S. Ye, Y. Zhang, *Front. Phys.* **2021**, *500*, 351.

[50] J. Yang, L. Xu, G. Z. Zhang, R. X. Mao, Z. P. Yin, H. B. Lu, G. S. Deng, Y. Li, *Opt. Express* **2022**, *30*, 17361.

[51] S. Savo, D. Shrekenhamer, W. J. Padilla, *Adv. Opt. Mater.* **2014**, *2*, 275.

[52] C. J. Gao, D. Zhang, H. F. Zhang, *Ann. Phys.* **2022**, *534*, 2100578.

[53] H. Li, W. Xu, Q. Cui, Y. Wang, J. Yu, *Opt. Express* **2020**, *28*, 40060.

[54] N. Shao, S. Y. Wang, G. Y. Wen, *Appl. Phys. A: Mater. Sci. Process.* **2018**, *124*, 525.

[55] X. X. Wu, Y. Meng, L. Wang, J. X. Tian, S. W. Dai, W. J. Wen, *Appl. Phys. Lett.* **2016**, *108*, 183502.

[56] F. Bilotti, A. Toscano, L. Vegni, K. Lucio, K. Aydin, K. B. Alici, E. Ozbay, *IEEE Trans. Microwave Theory Tech.* **2007**, *55*, 2865.

[57] Y. Liu, X. Bai, G. Yao, *J. Opt. Soc. Am. B* **2018**, *35*, 1005.

[58] N. H. Shen, M. Massaouti, M. Gokkavas, J. M. Manceau, E. Ozbay, M. Kafesaki, T. Koschny, S. Tzortzakis, C. M. Soukoulis, *Phys. Rev. Lett.* **2011**, *106*, 037403.

[59] Y. Yang, I. I. Kravcheko, D. P. Briggs, J. Valentine, *Nat. Commun.* **2014**, *5*, 5753.

[60] D. X. Yan, Q. Y. Feng, Z. W. Yuan, M. Meng, X. J. Li, G. H. Qiu, J. N. Li, *Chin. Phys. B* **2022**, *31*, 014211.

[61] Y. P. Li, L. Zeng, H. F. Zhang, D. Zhang, K. Xia, L. Zhang, *Opt. Express* **2022**, *30*, 34586.

[62] X. Y. Yu, X. Gao, W. Qiao, L. L. Wen, W. L. Yang, *IEEE. Photonics Technol. Lett.* **2016**, *28*, 2399.

[63] H. L. Zhu, Y. Zhang, L. F. Ye, Y. K. Li, Y. H. Xu, R. M. Xu, *Opt. Express* **2020**, *28*, 38626.

[64] D. W. Yu, Y. F. Dong, Y. D. Ruan, G. C. Li, G. S. Li, H. M. Ma, S. Deng, Z. P. Liu, *Crystals* **2021**, *11*, 1116.

[65] S. Y. Liao, J. Y. Sui, H. F. Zhang, *Opt. Express* **2022**, *30*, 34172.

[66] M. Barkabian, N. Sharifi, N. Granpayeh, *Opt. Express* **2021**, *29*, 20160.

[67] H. J. Zhang, Y. Liu, Z. Q. Liu, X. S. Liu, G. Q. Liu, G. L. Fu, J. Q. Wang, Y. Shen, *Opt. Express* **2021**, *29*, 70.